Research Article

Štefan Hardoň*, Jozef Kúdelčík, Marián Janek, Anton Baran, Alena Kozáková and Tomáš Dérer

Halloysite nanotube enhanced polyurethane nanocomposites for advanced electroinsulating applications

https://doi.org/10.1515/ntrev-2025-0248
Received July 29, 2025; accepted November 4, 2025;
published online December 4, 2025

Abstract: Halloysite nanotubes (HNT), as naturally occurring anisotropic nanofillers, were incorporated into a commercial two-component (2C) polyurethane (PU) system to develop multifunctional nanocomposites for electroinsulating applications. The nanocomposites were prepared via the method of direct dispersion. Dielectric, thermal, and mechanical properties were systematically analyzed at weight concentrations of 2 wt%, 5 wt%, and 10 wt% of HNT in the PU matrix. At 5 wt% HNT, an optimal balance was observed: volume resistivity increased nearly 17-fold, dielectric permittivity was enhanced through Maxwell–Wagner–Sillars interfacial polarization, and thermal conductivity rose modestly while maintaining high mechanical integrity. Broadband dielectric spectroscopy, modeled using the Havriliak–Negami function, showed broadened relaxation dynamics associated with filler–matrix interfaces. Incorporation of 10 wt% HNT caused agglomeration, reducing property uniformity. The results demonstrate that controlled integration of HNT into cold-curing 2C PU systems yields cost-effective, sustainable, and high-performance nanodielectrics, advancing their potential use in high-voltage insulation, aerospace encapsulation, and battery module safety.

Keywords: halloysite nanotubes; polyurethane nanocomposites; dielectric properties; thermal conductivity; mechanical reinforcement

***Corresponding author: Štefan Hardoň**, Department of Physics, Faculty of Electrical Engineering and Information Technology, University of Žilina, Univerzitná 8215/1, Žilina, Slovak Republic, E-mail: stefan.hardon@uniza.sk
Jozef Kúdelčík and Marián Janek, Department of Physics, Faculty of Electrical Engineering and Information Technology, University of Žilina, Univerzitná 8215/1, Žilina, Slovak Republic
Anton Baran, Department of Physics, Faculty of Electrical Engineering and Informatics, Technical University of Košice, Park Komenského 2, Košice, Slovak Republic
Alena Kozáková and Tomáš Dérer, VUKI a. s., Electroinsulating Resins and Varnishes, Pri majeri 1, 831 07, Bratislava 36, Slovak Republic

1 Introduction

Two-component PU systems are widely employed as potting materials and electrical insulators in high-voltage electronics, power systems, and aerospace platforms, owing to their outstanding dielectric strength, chemical resistance, thermal stability, and mechanical resilience. As operational demands intensify, particularly in environments involving elevated temperatures, electrical stress, or mechanical strain, there is a critical need to develop PU systems with multifunctional capabilities that extend beyond traditional performance limits.

Among the most promising strategies for performance enhancement is the incorporation of nanostructured fillers. HNT, naturally occurring aluminosilicate minerals with a hollow tubular morphology, have gained attention as effective nanofillers due to their low cost, biocompatibility, anisotropic geometry, and favorable surface chemistry. The outer siloxane (Si–O–Si) and inner aluminol (Al–OH) surfaces of HNT enable distinct charge separation and chemical reactivity, which facilitate interfacial adhesion, tailored functionalization, and stable dispersion within polymer matrices [1–4].

HNT, with the chemical formula $Al_2Si_2O_5(OH)_4 \cdot nH_2O$, exists in hydrated (10 Å) and dehydrated (7 Å) forms depending on thermal treatment [5]. Morphologically, HNT resemble multi-walled carbon nanotubes (MWCNTs), but offer substantial advantages in terms of environmental compatibility, cost-effectiveness, and ease of processing [2]. Their high aspect ratio and mesoporous architecture contribute not only to mechanical reinforcement, but also to the development of tortuous conduction pathways and enhanced barrier properties – key factors in improving thermal and dielectric behavior in nanocomposites.

Numerous studies have shown that HNT improve the thermal and electrical properties of polymer systems, including epoxy, polyethylene, and polyaniline. For example,

Bertolino et al. demonstrated that HNT enhanced oxidative thermal stability in multilayer biofilms due to their compacted tubular structure [1]. Similarly, in epoxy/HNT composites, Hornak et al. observed suppression of thermo-oxidative degradation alongside improved dielectric stability [6], while other recent studies have confirmed enhanced thermal conductivity, dielectric strength, and long-term electrical reliability in HNT-filled systems [7–13].

Moreover, the emergence of additive manufacturing has accelerated the development of smart, responsive nanocomposites. Recent 3D and 4D printing studies involving PLA-TPU or PLA-PBAT-Fe_3O_4 blends show that nanoscale fillers contribute not only to stiffness and conductivity, but also to shape memory behavior and thermal programmability [14–16]. These findings, though based on thermoplastic matrices, underscore a universal design principle: when uniformly dispersed and strongly bonded, nanoscale reinforcements serve as active elements that govern the multifunctional response of polymer systems.

Despite these advances, the systematic incorporation of HNT into commercial grade two-component PU systems remains underexplored. The existing literature focuses predominantly on thermoplastics or lab-synthesized matrices, whereas industrial formulations, especially cold-curing systems, pose different challenges in terms of filler compatibility, phase separation, and processing-induced voids.

Recent theoretical and experimental studies [2, 5, 11, 17–22] have underscored the pivotal role of HNT as architecturally active nanofillers that significantly influence the multifunctional performance of polymer nanocomposites. Their anisotropic structure and dual surface polarity, aluminol groups on the inner lumen and siloxane groups on the outer surface, not only promote interfacial polarization and charge trapping but also enhance matrix compatibility and facilitate the formation of percolated interphase domains. Compared to conventional fillers such as silica or carbon nanotubes, HNT often exhibit superior performance due to their natural tubular morphology and high aspect ratio [23, 24], though achieving uniform dispersion and robust interfacial bonding remains a critical challenge [25].

Furthermore, the present study addresses a notable discrepancy in prior literature, where some studies report optimal dielectric and mechanical enhancement at low HNT concentrations (~2 wt%) [6, 11, 20], while others suggest superior performance at higher loadings (~5–10 wt%) [3, 7, 8]. These inconsistencies, often arising from differences in matrix chemistry, dispersion quality, or measurement protocols, highlight the need for a systematic investigation under industrially relevant conditions.

The present work builds upon our previous investigations involving ZnO, Al_2O_3, and MgO nanoparticles [26–30], but advances the state of the art by integrating naturally abundant anisotropic HNT into a commercial two-component cold-curing PU matrix. In this context, HNT outperform conventional fillers due to their surface polarity, tubular anisotropy, and natural abundance, allowing for a cost-effective yet high-performance composite design. The rational integration of these nanofillers into industry-standard PU systems paves the way for multifunctional materials aligned with energy efficiency, durability, and sustainability goals in next-generation electrical insulation technologies.

2 Experimental section

2.1 Materials

HNT were used as received from Sigma-Aldrich (Product No. 685445, St. Louis, MO, USA). These naturally occurring aluminosilicates have the chemical composition $Al_2Si_2O_5(OH)_4 \cdot nH_2O$ and exhibit unique hollow tubular morphology with an outer diameter of 50–70 nm, inner diameter of 15–20 nm, and lengths spanning 1–3 μm (BET surface area ≈ 64–65 m^2/g; density ≈ 2.53 g/cm^3; thermal dehydration near 300 °C) [31]. Their inherent structure, characterized by robust hydrogen bonding and lower surface hydroxyl reactivity compared to inner lumen groups, confers excellent thermal stability and suppresses undesirable conductive pathways, making them ideal for integration into insulating polymer matrices.

The PU system used in this study was a commercial two-component potting compound known as VUKOL N22 Magna Blue, designed primarily for the encapsulation of electrical components [32]. It provides mechanical protection, electrical insulation, limited environmental resistance, and exhibits self-extinguishing behavior under fire exposure. The formulation consists of two liquid components: Component A (polyol) and Component B (curing agent), which must be mixed in a prescribed weight ratio of 100:47.

The initial mixture is characterized by low viscosity, making it suitable for casting into removable molds or permanent enclosures. The Component A also contains proprietary additives to tailor processing and end-use properties, including flame retardants (UL94 V-2 flammability classification at a thickness of 2 mm) and a blue pigment (specific to the Magna Blue variant). Upon mixing, a chemical reaction occurs between the hydroxyl (–OH) groups of a multifunctional polyol (component A, derived from castor oil) and the isocyanate (–NCO) groups of a curing agent (component B, based on diphenylmethane diisocyanate, MDI, and its oligomers). Component A typically contains three –OH groups per molecule, while component B provides two –N=C=O functionalities

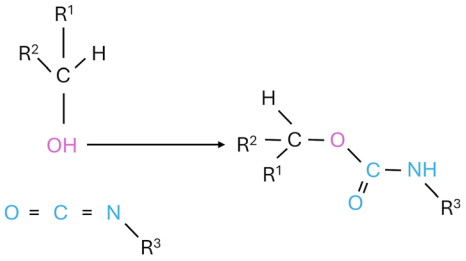

Figure 1: Chemical reaction of urethane bond formation.

per molecule. This stoichiometry facilitates the formation of extended urethane linkages, ultimately resulting in a highly cross-linked, three-dimensional (3D) polymer network. The resulting structure imparts a viscoelastic and semi-rigid character to the cured polyurethane matrix, which is critical for applications requiring a balance of mechanical integrity and dielectric insulation. The material undergoes gradual gelation over several tens of minutes depending on the layer thickness and heat dissipation, and requires at least 10 days at room temperature to achieve full cure. The resulting polymer is insoluble in solvents, thermoset (non-meltable), and demonstrates slow, partial recovery upon mechanical deformation (Figure 1).

From a structural perspective, the formulation includes additional cross-linking agents that facilitate the development of a densely interconnected polymer network during curing, thereby enhancing its mechanical integrity. As a result, the cured material exhibits improved toughness and hardness, with a Shore A value in the range of 77–80. Its low initial viscosity is particularly advantageous for precision casting into narrow voids and complex geometries, making it suitable for advanced electrical insulation and thermal management applications.

Beyond laboratory evaluation, this two-component PU system is also applied in commercial-scale energy storage systems, where it serves as an encapsulant and structural insulator for battery modules. Its favorable rheological properties promote efficient infiltration into confined cell compartments and interstitial spaces, ensuring uniform encapsulation. Upon curing, the material contributes to mechanical stabilization, enhances resistance to vibrational and thermal cycling stresses, and supports overall operational safety and durability. The integration of such PU systems into battery technologies highlights their multifunctional utility and relevance for next-generation electrochemical energy storage applications.

2.2 Fabrication of PU/HNT nanocomposites

The nanocomposites were prepared using a dispersive mixing technique optimized to ensure a uniform distribution of HNT within a two-component polyurethane (2C-PU) matrix. We successfully employed the method of direct dispersion in the preparation of nanocomposite samples, as described also in our previous works [26–30, 33]. All HNT were vacuum-dried (Thermo Scientific, Vacutherm, model VT 6025, Germany) at 40 °C for 24 h to remove adsorbed moisture prior to use. The required amount of HNT (2, 5, or 10 wt%) was dispersed into Component A (polyol) and subjected to mechanical stirring using a magnetic stirrer at 700 rpm for 3 h at 40 °C to optimize viscosity.

To further minimize agglomeration, the suspension was exposed to ultrasonication for 1 h using a high-frequency needle-type sonicator (Bandelin, Sonopuls, Germany, 20 kHz). This step was followed by vacuum degassing at 10 mPa for 1 h to eliminate entrapped air bubbles. The isocyanate hardener (Component B) was then added in a 100:47 weight ratio and mixed using magnetic stirring at 100 rpm for 3 min under concurrent vacuum degassing.

The resulting homogeneous mixture was poured into circular silicone molds and cured under ambient laboratory conditions (23 °C, 50 % RH) for 48 h. All specimens were prepared in 10 replicates to ensure measurement reproducibility and statistical significance (Figure 2). Reference PU samples were processed under identical mixing, curing, and conditioning conditions, with the only difference being the absence of HNT fillers.

The reference PU samples were processed under mixing, curing, and conditioning conditions identical to those of the nanocomposites, with the only difference being the absence of HNT fillers.

3 Results and discussion

3.1 Dynamic mechanical analysis

The dynamic mechanical analysis (DMA) of polymeric materials is highly sensitive to molecular mobility, which undergoes significant changes during relaxation transitions such as the glass transition (T_g) and secondary relaxations. The glass transition temperature is commonly identified as the peak in the temperature dependence of the loss factor ($\tan \delta$), corresponding to the onset of cooperative segmental motion in the amorphous domains. At this temperature, polymer chains transition from a glassy, rigid state to a rubber-like, flexible regime.

DMA measurements were conducted using a TA Instruments Q800 analyzer (Eschborn, Germany) operated in tension mode. DMA measurements were performed once. The glass transition temperatures were determined with error ±1 °C. A sinusoidal deformation with an

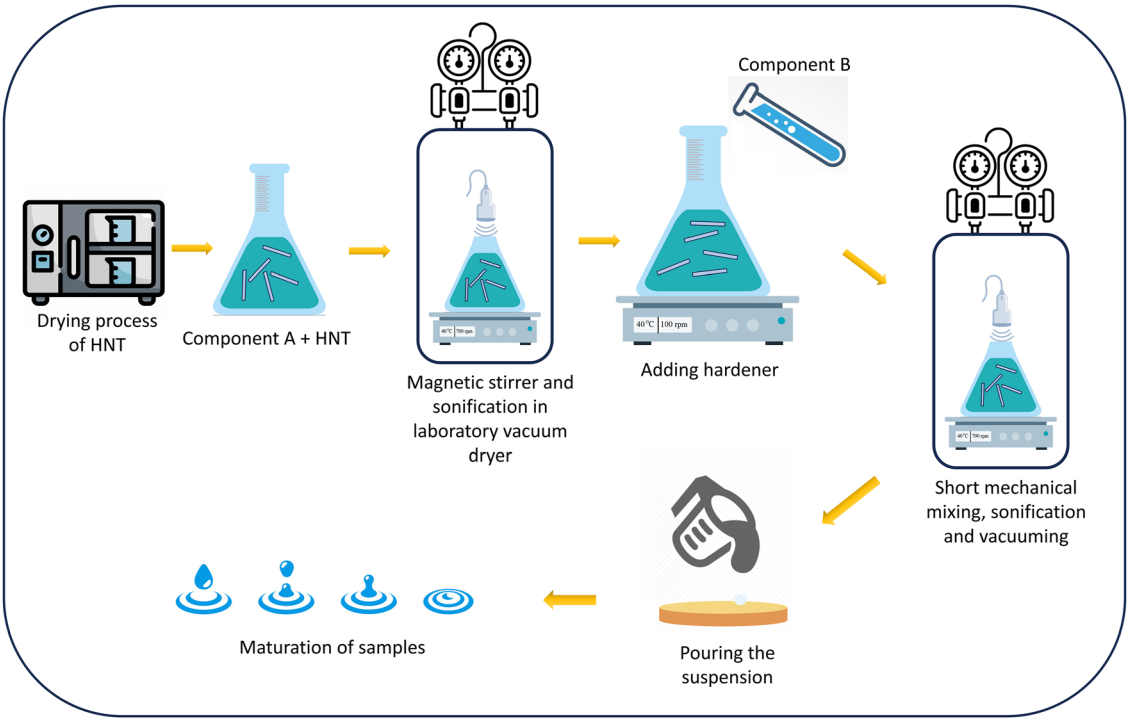

Figure 2: Schematic illustration of the HNT composites preparation.

amplitude of 5 µm was applied at a fixed frequency of 5 Hz. Samples of 1 mm thickness and 8 mm width were heated from −50 °C to 80 °C at a uniform rate of 2 °C/min under a nitrogen atmosphere to minimize the oxidative effects.

The temperature-dependent behavior of the storage modulus and loss factor (tan δ) for the pure PU matrix and its HNT – based nanocomposites is presented in Figure 3. The nanocomposites containing 2 wt% (PU + 2 % HNT) composite exhibited a lower storage modulus than pure PU, indicative of reduced stiffness and brittleness. Moreover, a slight shift of T_g toward lower temperatures was observed in the tan δ profile, suggesting enhanced chain mobility. This effect is attributed to increased phase separation and the formation of hydrogen bonds between urethane groups in the hard segments of the polyurethane and hydroxyl groups located on the HNT surface. These interactions likely disrupt segmental miscibility and increase free volume, thereby enhancing the mobility of soft segments [34]. This interpretation is further supported by ^{1}H NMR measurements (Figure 5) performed on PU nanocomposites with varying HNT loadings [35].

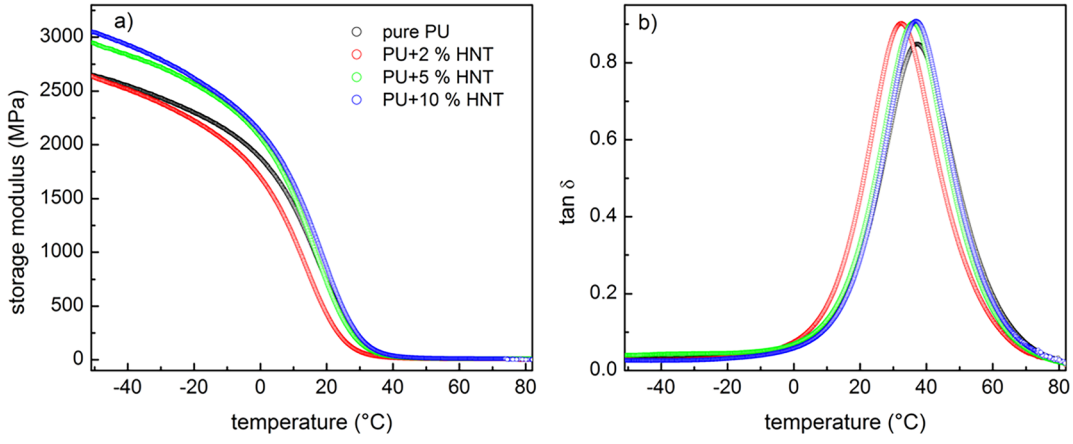

Figure 3: Temperature dependence of storage modulus (a) and loss factor tan δ (b) for pure PU and its nanocomposites with varying HNT content.

In contrast, nanocomposites containing 5 wt% (PU + 5 % HNT) and 10 wt% (PU + 10 % HNT) HNT demonstrated consistently higher storage moduli across the examined temperature range, indicating increased rigidity and brittleness. The T_g values of these samples remained close to those of pure PU. At elevated HNT content, the likelihood of filler agglomeration increases, which can hinder effective phase separation and reduce the available free volume, thereby suppressing soft segment mobility and reinforcing the composite structure.

3.2 X-ray diffraction

XRD measurements were conducted using a Rigaku MiniFlex600 diffractometer (Tokyo, Japan) operated at 40 kV and 15 mA with CuKα radiation (λ = 0.154 nm). The measurements employed the θ–2θ configuration with scan rates of 2.5°/min for the sample and 5°/min for the detector. Baseline correction was applied to all collected diffractograms to enhance signal clarity and comparability.

Figure 4 presents the XRD patterns of pure HNT, unmodified PU, and HNT-reinforced PU nanocomposites. The XRD diffractogram of pure HNT exhibits distinct diffraction peaks at 2θ = 12.1°, 20.0°, 24.6°, 26.7°, 35.1°, 38.1°, and 54.1°, which are characteristic of the crystalline structure of halloysite and consistent with previous reports [36–38].

The diffractogram of pure PU reveals two broad diffraction features centered at 2θ = 12.1° and 20.7°. According to previous studies [39, 40], the broad peak of 20.7° corresponds to microcrystalline domains in the soft segments,

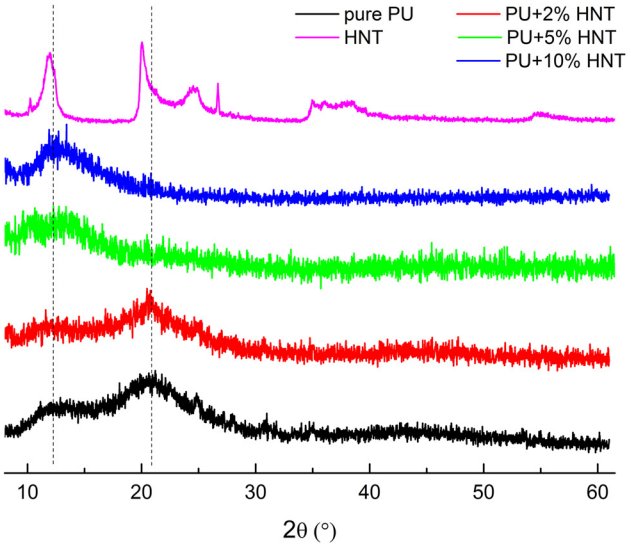

Figure 4: XRD patterns for pure HNT, pure PU, and their nanocomposites.

suggesting that the PU matrix is predominantly amorphous with dispersed microcrystalline inclusions. Reflection at 12.1° is attributed to short-range ordering in the hard segment domains, indicating the formation of microcrystals without long-range crystallinity [41, 42].

For the PU + 2 % HNT nanocomposite, the diffraction pattern closely resembles that of pure PU, indicating that incorporation of a low concentration of HNT does not significantly change of the PU matrix on the larger scale. At this filler loading, no distinct peaks associated with crystalline HNT are observed, likely due to their low volume fraction and uniform dispersion.

At higher HNT concentrations (5 wt% and 10 wt%), notable structural changes emerge. The diffraction peak at 2θ = 20.7° – associated with soft segment microcrystallinity – vanishes entirely, suggesting that the increased filler content disrupts the ordering of soft domains. In contrast, the intensity of the peak at 12.1°, associated with hard segments, increases relative to pure PU. This observation may reflect the restricted mobility of polymer chains in the presence of HNT aggregates, which hinder soft segment packing while facilitating localized ordering of hard segments. The enhanced peak intensity may indicate an increase in the size or population of microcrystalline domains due to interfacial interactions between HNT and the hard segments of the PU matrix.

3.3 ^{27}AI nuclear magnetic resonance

Solid-state NMR measurements were conducted on a Varian 400 MHz spectrometer (Palo Alto, CA, USA). The ^{27}Al spectra were recorded at a Larmor frequency of 104.17 MHz using a π/6 pulse excitation (1.05 µs pulse width), a recycle delay of 1 s, and a magic-angle spinning (MAS) rate of 12 kHz. Each spectrum included 3,600 scans. A 1 mol/L aqueous solution of $[Al(H_2O)_6]^{3+}$ was used as an external chemical shift reference.

^{27}AI nuclear magnetic resonance spectroscopy is highly sensitive to the aluminum coordination environment, particularly the coordination number and local geometry surrounding the Al nuclei. These structural factors produce well-defined chemical shift regions that correspond to distinct AlO_x environments in aluminosilicates and related frameworks [43]. Accordingly, ^{27}Al NMR provides valuable insight into the dispersion state and interfacial interactions of HNT embedded within a PU matrix.

Figure 5 displays the ^{27}Al MAS NMR spectra obtained at room temperature for pure HNT and the corresponding PU-based nanocomposites. The spectrum of the unmodified HNT shows a single, symmetric resonance centered at

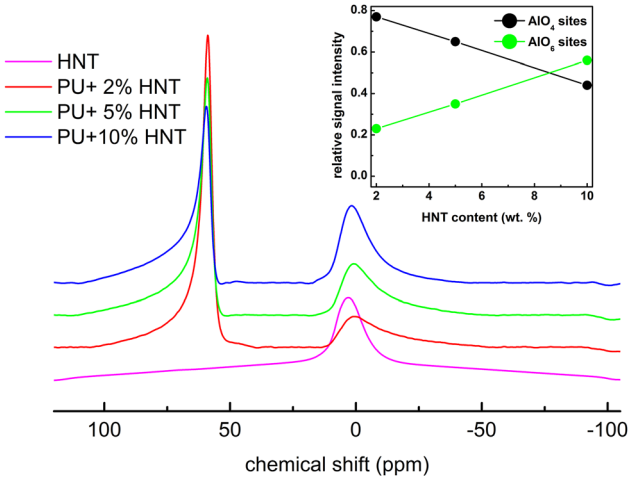

Figure 5: ^{27}Al NMR spectra for pure HNT and polyurethane nanocomposites measured at ambient temperature. Inset shows dependence of relative signal intensity assigned to ^{27}Al nuclei in AlO_6 and AlO_4 sites versus concentration of HNT in studied nanocomposites.

3.2 ppm, consistent with the presence of octahedral coordinated aluminum species (AlO_6). In contrast, all PU/HNT nanocomposites exhibit an additional resonance near 60 ppm, attributed to tetrahedrally coordinated AlO_4 sites.

These spectral differences arise from modifications in local symmetry and disorder at the aluminum sites, likely caused by chemical interactions with the surrounding polymer. The appearance of the AlO_4 signal at 60 ppm is consistent with the hydrogen bond between hydroxyl groups on the HNT surface and urethane groups in the polymer, which induces partial dehydroxylation and structural rearrangement, an effect analogous to thermally driven dehydroxylation observed in prior studies [44].

Furthermore, the relative intensity of the AlO_4 resonance systematically decreases with increasing HNT content. Specifically, for nanocomposites containing 2 wt%, 5 wt%, and 10 wt% HNT, the relative intensities of the tetrahedral AlO_4 sites are 0.77, 0.65, and 0.44, respectively. This trend suggests that at higher filler loadings, the formation of HNT aggregates limits interfacial contact with the polymer, thereby preserving the original AlO_6 coordination environments within the HNT structure. The micrograph for the 10 wt% sample shows a marked area of HNT agglomeration, indicating compromised dispersion quality at higher filler loading.

3.4 Elemental analysis by energy-dispersive X-ray spectroscopy (EDS)

The EDS composite analysis of the PU nanocomposite with 2 wt% HNT (Figure 6) confirms the incorporation and spatial distribution of HNT within the PU matrix. The spectrum reveals dominant carbon (C) and oxygen (O) peaks originating from the organic PU host, along with distinct

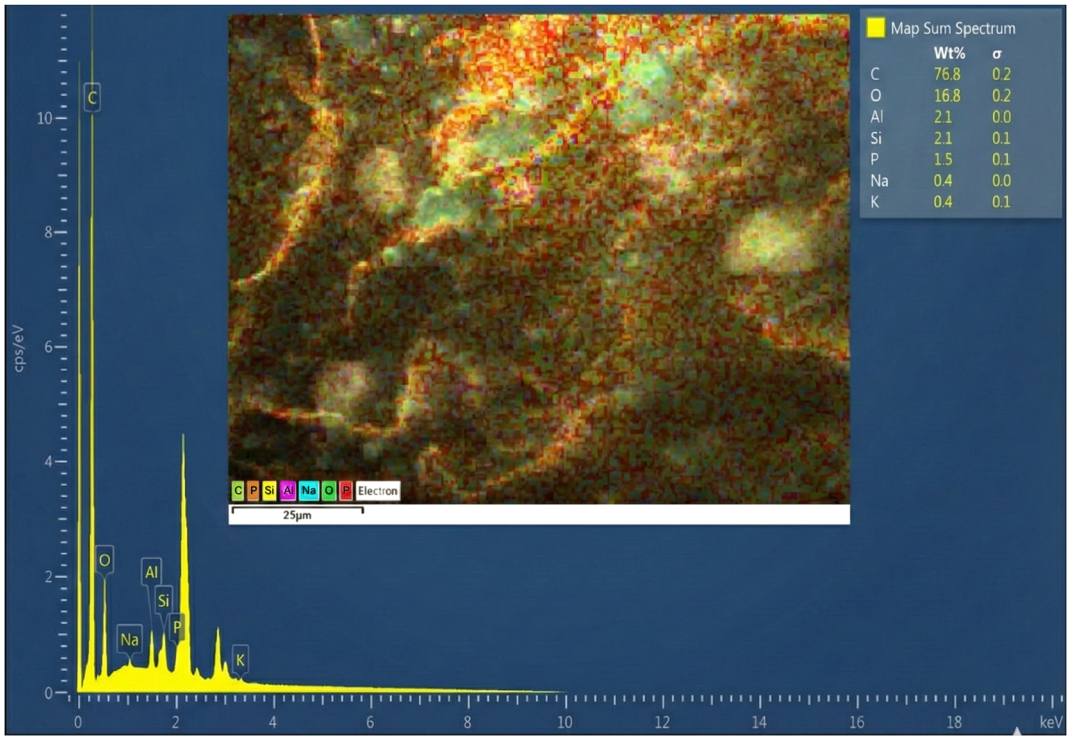

Figure 6: EDS elemental mapping of the PU nanocomposite filled with 2 wt% HNT, showing the spatial distribution of C, O, Al, Si, P, and trace elements. HNT are identified via co-localized Al and Si domains within the polyurethane matrix.

aluminum (Al) and silicon (Si) peaks that are characteristic of the $Al_2Si_2O_5$ structure of HNT. A phosphorus (P) signal corresponds to a flame-retardant additive, while minor amounts of sodium (Na) and potassium (K) likely reflect the residual mineral components inherent to natural halloysite. The embedded EDS map inset illustrates the co-localization of Al and Si within localized domains, confirming the spatial distribution of HNT-rich clusters. The continuous carbon background, together with these discrete filler zones, supports the conclusion that HNT are effectively dispersed, though not fully homogenized within the PU matrix.

3.5 Fourier transform infrared spectroscopy analysis of PU/HNT

Fourier Transform Infrared (FTIR) spectroscopy is a widely applied analytical technique for identifying functional groups and monitoring molecular interactions in polymer-based systems. It provides information about the vibrational modes of chemical bonds and enables detection of structural changes in materials at the molecular level. In studies of polymer nanocomposites [22, 45], FTIR is particularly useful for confirming the presence of specific fillers, tracking variations in characteristic absorption bands, and evaluating possible interactions at the matrix–filler interface. By analyzing the position, intensity, and shape of absorption peaks, valuable insights can be obtained into chemical bonding, hydrogen interactions, and compatibility between the polymer matrix and nanofillers.

The macroscopic assessment of the dispersion homogeneity of HNT fillers within the specimens was performed using FTIR spectroscopy in transmission mode, employing a Nicolet 380 spectrometer (Thermo Scientific, USA). The broadening and slight shifts observed in the N–H stretching at approximately 3,300 cm^{-1} and the C=O stretching of urethane groups around 1,700–1,730 cm^{-1} suggest the presence of hydrogen bonding between surface hydroxyl groups of HNT and the urethane functionalities of the polymer. These interactions are consistent with the known surface chemistry of halloysite, where the inner lumen (Al–OH groups) is positively charged and the outer surface (Si–O–Si groups) carries a negative charge. This polarity promotes multiple bonding mechanisms, including hydrogen bonding between N–H groups of urethane and hydroxyl groups on the HNT surface, dipole–dipole interactions between polar carbonyl groups of the polyurethane and the negatively charged Si–O–Si surface of HNT, as well as electrostatic interactions between positively charged Al–OH inner lumen groups and polar moieties of the polymer. At higher HNT contents (5–10 %), these interactions become more evident in the spectra, as indicated by band broadening in both the urethane group region and the C–O–C vibration range (1,100–1,300 cm^{-1}), where overlap with HNT signals occurs, Figure 7. These findings suggest that HNT acts not only as a passive filler but also as an active component capable of forming physical bonds with the polyurethane matrix, improving interfacial adhesion and potentially influencing the dielectric and mechanical behavior of the nanocomposites.

3.6 Volume resistivity

The evaluation of volume resistivity serves as a critical diagnostic tool for assessing the dielectric integrity of polymer-based nanocomposites, particularly in high-voltage

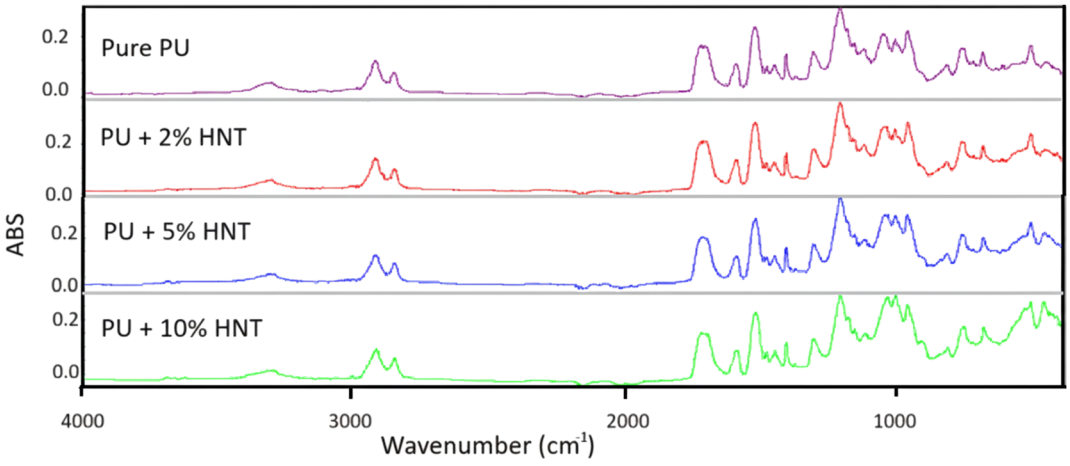

Figure 7: FTIR spectra of pure PU and PU/HNT nanocomposites with varying HNT content, illustrating characteristic PU bands and the emerging Si–O–Si and Al–O signals of HNT.

applications where suppression of leakage currents and long-term insulation reliability are paramount. This parameter reflects the ability of the material to maintain electrical resistance under sustained DC stress and is strongly influenced by interfacial phenomena and filler dispersion quality.

All measurements were conducted in accordance with the IEC 62631-3-1 and IEC 62631-3-2 standards using a Keithley 6517A electrometer coupled with a Keithley 8009 resistivity test fixture (Keithley Instruments, OH, USA). Prior to testing, all specimens were conditioned under short-circuit conditions for 24 h to ensure measurement stability. For evaluation, five independently prepared samples were measured to ensure reproducibility and statistical reliability. In this study, the unmodified PU matrix exhibited an intrinsic volume resistivity of $5.38 \times 10^{14}\,\Omega\,m$ with a measurement error of 0.9 %, in agreement with literature data for insulating PU used in electrical potting and encapsulation [20, 46]. Upon incorporation of 2 wt% HNT, the resistivity increased substantially to $5.13 \times 10^{15}\,\Omega\,m$ with a measurement error of 0.7 %. The maximum enhancement was achieved at 5 wt% loading with a measurement error of 0.6 % and reaching $9.04 \times 10^{15}\,\Omega\,m$ an improvement of nearly 17-fold over the pure PU matrix (Figure 8). This significant rise is attributed to the formation of tortuous conduction pathways, interfacial polarization mechanisms (e.g., Maxwell–Wagner–Sillars effect, α-polarization), and space charge trapping induced by the high aspect ratio and insulating character of HNT.

However, at 10 wt% filler content, a decline in resistivity to $1.98 \times 10^{15}\,\Omega\,m$ with a measurement error of 1.0 % was observed. This reduction is likely due to nanotube agglomeration, which creates localized conduction pathways, diminishes interfacial area for polarization, and disrupts the homogeneity of the composite microstructure. The resulting compromise in dielectric uniformity highlights the importance of maintaining nanoscale dispersion to preserve high insulation performance.

Notably, current stabilization was only achieved after approximately 60 min of continuous DC voltage application, indicating the presence of dominant absorption currents in the early stages of measurement. These currents originate from interfacial dipole alignment, molecular polarization, and delayed carrier drift. Such a transient behavior is characteristic of highly resistive nanodielectrics, particularly those containing deep trap states and extended interfacial regions introduced by nanofillers [20, 47, 48]. These features contribute to delayed ohmic conduction, reinforcing the insulating character of the material [27, 49–54].

Compared to previously reported PU/HNT composites, the values obtained in this work, particularly at 5 wt% filler, exceed the typical volume resistivity range (10^{13}–$10^{15}\,\Omega\,m$), underscoring the effectiveness of the filler–matrix interface and dispersion strategy employed. Moreover, composites exceeding $10^{15}\,\Omega\,m$ are typically classified as high-performance dielectrics suitable for critical applications such as high-voltage insulation, electric mobility, and battery module encapsulation.

3.7 Broadband dielectric spectroscopy

A dielectric spectroscopy setup using a three-electrode configuration [55–58] and was utilized for the measurement of basic dielectric parameters. In the frequency range of 100 Hz to 1 MHz, an OT 7600 Plus LCR meter (QuadTech, USA) was used to determine the real part of the capacitance and the bulk resistivity. For the low-frequency interval between 1 mHz and 10 kHz, complex capacitance and dissipation factor (tg δ) were recorded using an IDAX 350 precision analyzer (Megger, Sweden). All measurements were carried out according to the IEC 62631-2-1: 2018 standard [48], under controlled thermal conditions with a temperature stability of ±0.5 °C throughout the measurement protocol.

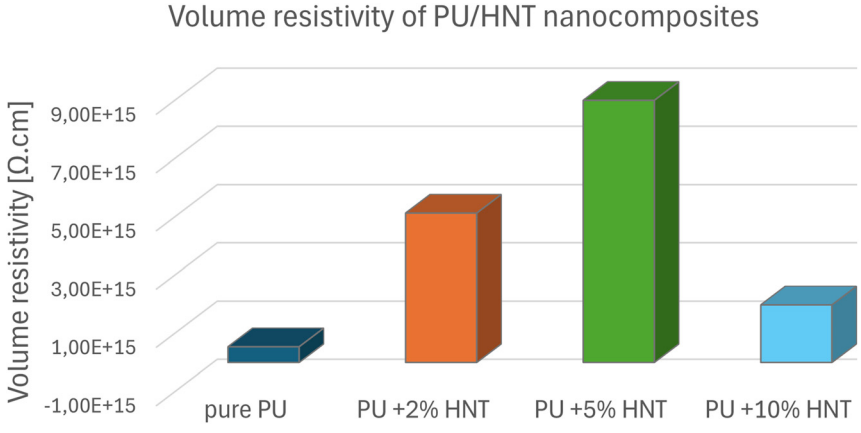

Figure 8: A bar chart comparing the volume resistivity ($\Omega \cdot m$) of PU/HNT composites.

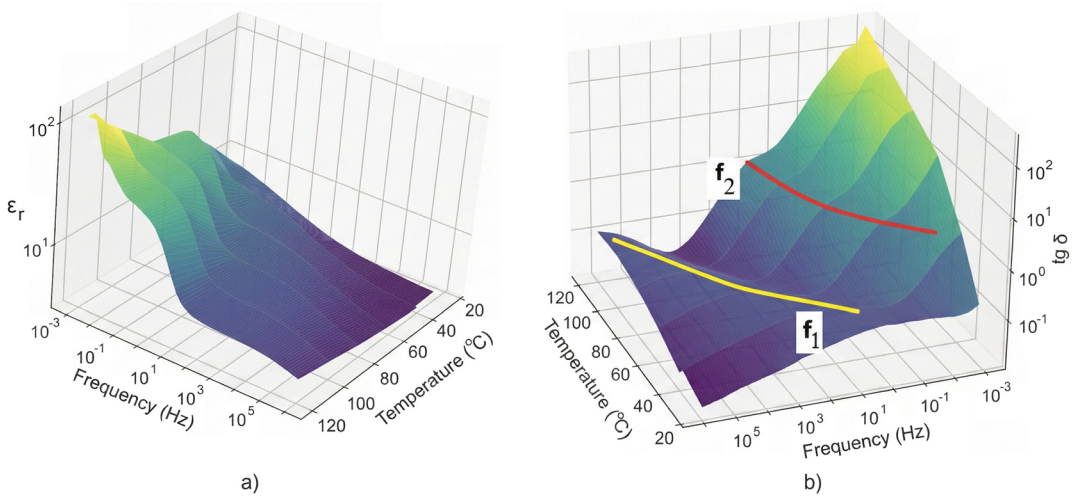

Figure 9: The frequency dependence (a) of the real part of the complex relative permittivity and (b) of the dissipation factor for PU with 2 wt% HNT nanoparticles.

Figure 9a displays the frequency-dependent real permittivity (ϵ_r) of PU reinforced with 2 wt% HNT nanoparticles, measured across temperatures from 25 °C to 120 °C over a frequency range of 1 mHz to 1 MHz. At 25 °C, ϵ_r increases from 3.5 to 7.6 as the frequency decreases to 1 mHz. At temperatures over 40 °C and below 1 Hz, a substantial temperature-dependent increase in ϵ_r is observed, which is attributed to enhanced electrode polarization.

The dissipation factor (tg δ) data reveals two distinct relaxation processes Figure 9b. The first, denoted as f_1, is linked to the intermediate dipolar effect (IDE) and shows a local maximum near 1 Hz at 25 °C. This maximum shifts to higher frequencies as the temperature increases. Above 60 °C, a second local maximum, f_2, appears in the sub-hertz range. This α-relaxation mode is associated with the glass transition and micro-Brownian motion of the polymer, and it also shifts to higher frequencies with increasing temperature. An increase in tgδ at very low [46, 59] or SiO_2 [29].

Figure 10 compares the real permittivity (a) and dissipation factor (b) of pure PU and PU with three different weight percent (wt%) concentrations of HNT fillers at 60 °C. Notably, PU with 2 wt% HNT exhibited lower permittivity across all frequencies compared to pure PU. Since nanotubes have a large active surface area, they can bind the hard segments located on the HNT surface, which reduces their mobility and therefore permittivity. The decrease in movement of the hard segments was also confirmed by DMA method Figure 3. A similar decrease in permittivity was observed for admixtures of MgO, ZnO, and SiO_2 nanoparticles at concentrations up to 1 wt% [46, 59]. Conversely, PU with 5 wt% HNT showed higher permittivity, particularly at frequencies above 5 Hz. This enhancement can be attributed to the role of HNT in promoting interfacial polarization (Maxwell–Wagner–Sillars effect). Due to their anisotropic tubular morphology and distinct surface polarity – aluminol groups on the inner lumen and siloxane groups on the outer wall – HNT establish well-defined interfaces with the surrounding PU matrix. Under an applied electric field, these interfaces serve as trapping sites for space charges, leading to localized charge accumulation and elevated permittivity. Moreover, the strong filler matrix interactions limit the mobility of charge carriers, thereby reducing dielectric losses. This is evidenced by the observed decrease in the dissipation factor (Figure 9b) for HNT filled samples, particularly at intermediate frequencies. These findings confirm that the quality and morphology of the filler matrix interface play a pivotal role in tuning the dielectric behavior of PU nanocomposites.

To obtain deeper insight into the dielectric relaxation processes, the Havriliak–Negami model was applied, as it provides a phenomenological yet highly accurate framework for modeling complex relaxation behavior in disordered materials. This model generalizes the Cole–Cole and Davidson–Cole formalisms by introducing two shape parameters to account for both the symmetric and asymmetric broadening of relaxation peaks.

The generalized complex permittivity function is expressed as:

$$\varepsilon^*(\omega) = \varepsilon_\infty + \frac{\Delta\varepsilon_1}{\left[1 + (j\omega\tau_{01})^{\alpha_1}\right]^{\beta_1}} + \frac{\Delta\varepsilon_2}{\left[1 + (j\omega\tau_{02})^{\alpha_2}\right]^{\beta_2}} - j\frac{\sigma_{DC}}{\varepsilon_0\omega} \quad (1)$$

where:

– $\varepsilon^*(\omega)$ is the complex dielectric permittivity,

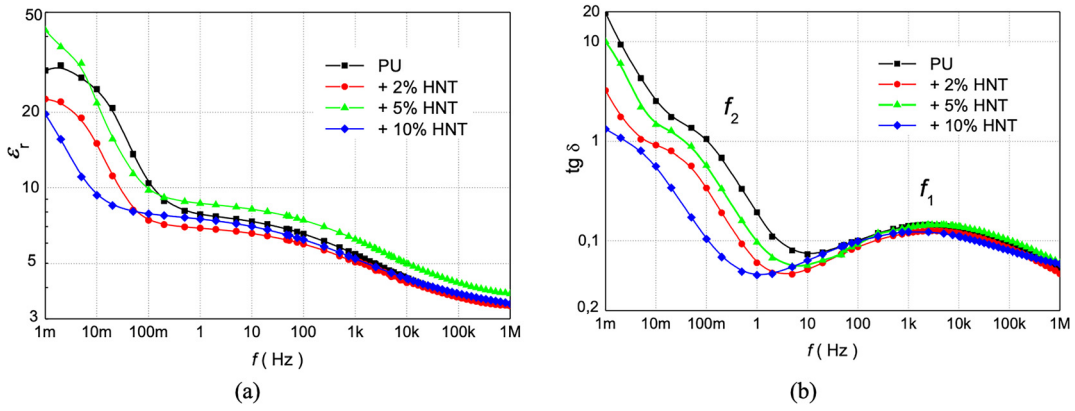

Figure 10: The frequency dependence (a) of the real part of the complex relative permittivity and (b) of the dissipation factor for PU with 2, 5 and 10 wt% HNT nanoparticles at a temperature of 60 °C.

- ε_∞ is the high-frequency limit of the permittivity,
- $\Delta\varepsilon$ is the dielectric strength ($\Delta\varepsilon = \varepsilon_s - \varepsilon_\infty$),
- τ_0 is the characteristic relaxation time,
- α and β are the empirical shape parameters ($0 < \alpha, \beta \leq 1$), governing symmetric and asymmetric peak broadening,
- σ_{DC} is the DC electrical conductivity,
- ε_0 is the permittivity of free space.

The double relaxation structure ($i = 1, 2$) was introduced due to the coexistence of distinct relaxation modes, attributed to interfacial (Maxwell–Wagner–Sillars) polarization and segmental mobility of polyurethane chains.

This model was selected on the basis of its demonstrated ability to fit broad and asymmetric dielectric loss peaks observed in polymer nanocomposites, particularly in systems with heterogeneous morphology and filler–matrix interactions. In this study, the HN model provided excellent agreement with experimental data across the measured frequency range (1 mHz–10 MHz), thereby enabling robust extraction of relaxation parameters associated with both dipolar and interfacial polarization mechanisms.

Table 1 summarizes the parameters fitted to the Havriliak–Negami model for these concentrations at a temperature of 60 °C. The addition of HNT reduces the DC conductivity what correspond with the increase of the volume resistivity (Figure 8). For all HNT concentrations (Figure 10b), the dissipation factor was smaller as pure PU at frequencies below 1 kHz. The addition of HNT decrease of value α_1, which confirms broader distribution of relaxation times due to increase in phase separation. Additionally, the α-mode relaxation peak (f_2) for the nanocomposites shifted to lower frequencies and is narrower (increase of α_2) as HNT content increased, indicating the restricted mobility of polymer chains in the presence of HNT aggregates (Figure 4. A significant shift of the whole development to lower frequencies due to particle agglomeration is observed in the case of 10 wt % HNT, f_2 is an order of magnitude smaller than for pure PU).

The results from broadband dielectric spectroscopy (BDS) strongly correlate with the volume resistivity trends, confirming that optimal HNT dispersion (at 2 and 5 wt%) leads to suppressed DC conductivity and reduced low-frequency dielectric losses [6, 60]. These effects are attributed to interfacial polarization, charge trapping, and increased tortuosity in the conductive pathways – mechanisms that also account for the observed 17-fold increase in resistivity. The shift of relaxation processes toward lower frequencies reflects reduced chain mobility and enhanced dielectric confinement. At 10 wt%, both BDS and resistivity data indicate a decline in

Table 1: Parameters of the Havriliak–Negami model for composites of various concentrations of HNT in PU at 60 °C, where $f = 1/(2\pi\tau)$, and α_1 is broadening parameter and β_1 is asymmetry parameter. Index 1 corresponds to the IDE process and index 2 to α-polarization.

Parameter	Pure PU	PU + 2 % HNT	PU + 5 % HNT	PU + 10 % HNT
ϵ_∞	3.0	3.1	3.3	3.0
σ (10^{-12} S/m)	31.6	3.94	12.2	1.11
Process 1: IDE Process				
$\Delta\epsilon_1$	4.6	4.1	5.4	4.8
τ_1 (ms)	0.649	0.198	0.276	1.11
f_1 (Hz)	245	803	577	143
α_1	0.51	0.38	0.43	0.381
β_1	0.57	0.95	0.77	0.69
Process 2: α Process				
$\Delta\epsilon_2$	23.5	16.1	15.3	15.9
τ_2 (s)	6.5	15.4	11.1	100.9
f_2 (mHz)	24	10	14	2
α_2	0.8	0.89	0.85	0.94
β_2	1	1	1	0.85

performance due to nanotube agglomeration, underscoring the critical role of filler dispersion in preserving electro-insulating functionality.

3.8 Analysis of PU HNT composite thermal conductivity

The results of our measurements show a slight and progressive increase in thermal conductivity with rising HNT concentration (Figure 11). Thermal conductivity measurements were initially conducted using a novel experimental setup developed for polyurethane composites [61], and subsequently verified using a TPS 2500 S thermal constants analyzer (Hot Disk AB, Sweden). This instrument enables high-precision determination of thermal conductivity, thermal diffusivity, and specific heat capacity in accordance with ISO 22007-2. Each reported value represents the average of 10 repeated measurements to ensure statistical reliability. The measured values are 0.200 W m^{-1} K^{-1} for pure PU, increasing to 0.213 W m^{-1} K^{-1} at PU + 2 % HNT, 0.220 W m^{-1} K^{-1} at PU + 5 % HNT, and finally 0.230 W m^{-1} K^{-1} in PU + 10 % HNT loading. The modest trend is consistent with findings reported in the scientific literature for solid polymer composites. This result demonstrates the effectiveness of HNT as a functional filler for enhancing the thermal transport properties of the polymer matrix.

The primary mechanism for this enhancement is the introduction of the HNT themselves, which possess a higher intrinsic thermal conductivity than the polyurethane matrix. Research shows that HNT can form effective thermal conductivity channels within the polymer [62].

These nanotubes act as “heat conduction bridges,” creating more efficient pathways for phonons, which are the primary carriers of heat in such materials [63]. One study on a solid polyurethane-based phase change material documented a significant increase in thermal conductivity from 0.111 W m^{-1} K^{-1} to 0.263 W m^{-1} K^{-1} with the addition of 5 wt% of functionalized HNT (HNTs@Fe_3O_4), attributing the improvement to the formation of these conductive pathways [42, 62].

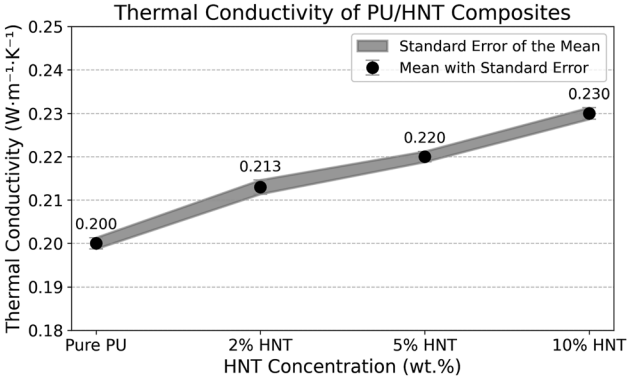

Figure 11: Thermal conductivity of PU/HNT composites. The data points represent the mean of 10 measurements, and the shaded area indicates the confidence band corresponding to the standard error of the mean.

The slight, progressive increase in thermal conductivity that we observed with rising HNT concentration (from 2 % to 10 %) is due to the formation of a more extensive and interconnected thermal network throughout the composite [64]. However, the effectiveness of this network is highly dependent on the quality of HNT dispersion and the interfacial bonding between the nanotubes and the polyurethane matrix. Good dispersion is crucial because agglomerated nanotubes can impede heat flow. Furthermore, a strong interaction at the filler-matrix interface is necessary to minimize interfacial thermal resistance (also known as Kapitza resistance), which can otherwise hinder efficient heat transfer [65]. While our data shows a modest, continued improvement up to 10 % loading, it is worth noting that some studies observe a diminishing rate of improvement at higher concentrations, as the challenges of maintaining good dispersion can begin to counteract the benefits of a denser filler network [62].

As illustrated in Figure 11, the progressive increase in thermal conductivity with HNT concentration is statistically discernible when considering the standard error of the mean across multiple measurements. Although the absolute increase is modest, the confidence bands for the different concentrations show minimal overlap, suggesting that the observed trend is not merely an artifact of experimental error. This provides stronger evidence that HNT create a more efficient thermal transport network within the polyurethane matrix.

3.9 Mechanical properties of HNT-reinforced polyurethane

Mechanical tests were carried out under controlled laboratory conditions at 25 °C to assess the tensile performance of HNT-reinforced polyurethane. For each material formulation, five replicate specimens were tested to ensure reproducibility and statistical reliability of the results. Uniaxial tensile tests were performed in accordance with the STN EN ISO 527-1 standard [66], using a constant crosshead speed of 50 mm/min. The final stress–strain curve for each formulation was obtained by averaging all replicative curves. The parameters evaluated included the ultimate tensile strength and elongation at break, corresponding to the maximum stress and strain values recorded prior to failure under monotonic loading.

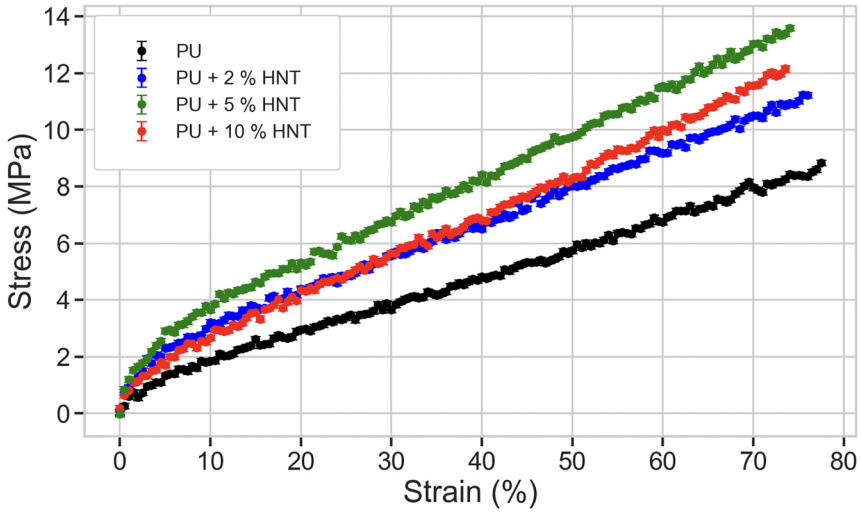

Figure 12: Stress–strain curves for pure PU, PU with 2 wt% HNT, 5 wt% HNT and with 10 wt% HNT.

Table 2: Values of tensile strength, elongation, and hardness of pure PU and its composites with HNT.

Oprule extbfSample	Tensile strength (MPa)	Elongation at break (%)	Hardness (Shore D)
PU	8.7	78.0	35
PU + 2 % HNT	11.2	76.6	40
PU + 5 % HNT	13.6	74.5	45
PU + 10 % HNT	12.1	73.9	45

All measurements were conducted using a Shimadzu AGS-X 50 kN (Japan) universal testing machine, equipped with high resolution load cells and automated data acquisition software. The experimental setup ensured consistent boundary conditions and accurate capture of force–displacement behavior across all test specimens. This methodology provided a robust basis for quantifying the effect of the incorporation of HNT on the mechanical performance of the polyurethane matrix.

The mechanical properties of pure PU and its nanocomposites containing 2 wt%, 5 wt% and 10 wt% of HNT were investigated to evaluate the effect of HNT loading on the polymer matrix. The tensile behavior of the materials is presented in the stress–strain curves in Figure 12, and the key mechanical parameters are summarized in Table 2, with the standard error not exceeding 0.3 MPa across all measurements.

Across the concentration series, all materials retained the characteristic ductile elastomeric profile of the base polyurethane, yet the incorporation of HNT systematically shifted the stress levels. Pure PU exhibited a Young's modulus of 39.9 MPa, an ultimate tensile strength of 8.7 MPa, and an elongation at break of 78 %. Introducing 2 wt% HNT produced a moderate reinforcement: the modulus increased to 55.0 MPa and the tensile strength reached 11.2 MPa, while the elongation at break decreased slightly to 76.6 %. These changes indicate efficient load transfer to the nanotubular filler and the onset of matrix stiffening [67, 68].

The composite containing 5 wt% HNT delivered the most pronounced enhancement. Its modulus climbed to 85.1 MPa and the tensile strength peaked at 13.6 MPa, a 56 % improvement over the neat matrix. Simultaneously, the elongation at break remained comparatively high (74.5 %), evidencing that the filler network reinforced the material without triggering brittle failure. Together with the observed Shore D hardness of 45, these findings pinpoint 5 wt% HNT as the optimal composition that balances stiffness, strength, and ductility.

At 10 wt% HNT the reinforcement effect begins to plateau. The modulus decreased to 70.0 MPa and the tensile strength fell to 12.1 MPa, albeit still above the neat PU. The additional filler fraction therefore yields diminishing returns, likely because localised agglomerates act as stress concentrators and partially disrupt load transfer [69–71]. The accompanying drop in elongation (73.9 %) and hardness (45 Shore D) supports this interpretation.

The concentration-dependent trends reinforce the importance of maintaining a percolated yet well-dispersed HNT network. Below 5 wt% the nanotubes are sufficiently separated to provide uniform reinforcement without sacrificing ductility, whereas higher loadings promote aggregate formation that undermines the mechanical synergy with the matrix. Consequently, 5 wt% HNT emerges as the most

advantageous formulation for applications requiring simultaneous gains in stiffness, strength, and hardness while preserving elastomeric extensibility.

3.10 Morphological analysis by scanning electron microscopy (SEM)

The fracture morphology of PU/HNT nanocomposites was systematically examined using scanning electron microscopy (SEM) to investigate the influence of HNT loading on filler dispersion, interfacial characteristics, and failure mechanisms. Clear morphological transitions were observed across the composition range, offering visual support for the structure–property relationships discussed throughout this study.

The pure PU matrix (Figure 13, top-left) displays a smooth and homogeneous surface devoid of particulate features, confirming the absence of inorganic inclusions and validating its use as a baseline.

At 2 wt% HNT loading (top-right), the fracture surface remains relatively smooth with isolated bright contrast regions corresponding to well-dispersed HNT. The lack of microvoids, pull-out structures, or significant crack propagation paths suggests effective stress dissipation and matrix continuity. This observation is consistent with DMA and dielectric spectroscopy results indicating enhanced chain mobility and suppressed DC conductivity.

The nanocomposite containing 5 wt% HNT (bottom-left) exhibits a more textured morphology with localized roughness, microcracks, and surface undulations, indicating stronger interfacial bonding and more efficient energy dissipation during fracture. The distribution of filler domains remains uniform, supporting the enhancements observed experimentally in thermal conductivity, volume resistivity, and tensile strength.

At 10 wt% HNT (bottom-right), pronounced nanoparticle clustering is visible, confirming the onset of agglomeration. The formation of filler-rich domains, reduced matrix continuity, and heterogeneous fracture topography indicate suboptimal dispersion. This morphology corroborates the mechanical and electrical performance decline observed at this concentration and validates the existence of a critical filler threshold beyond which interfacial quality and percolation effects dominate.

Overall, the SEM analysis provides direct microstructural evidence for the progressive transition from uniform dispersion to agglomeration, which underpins the nonlinear trends observed in dielectric, thermal, and

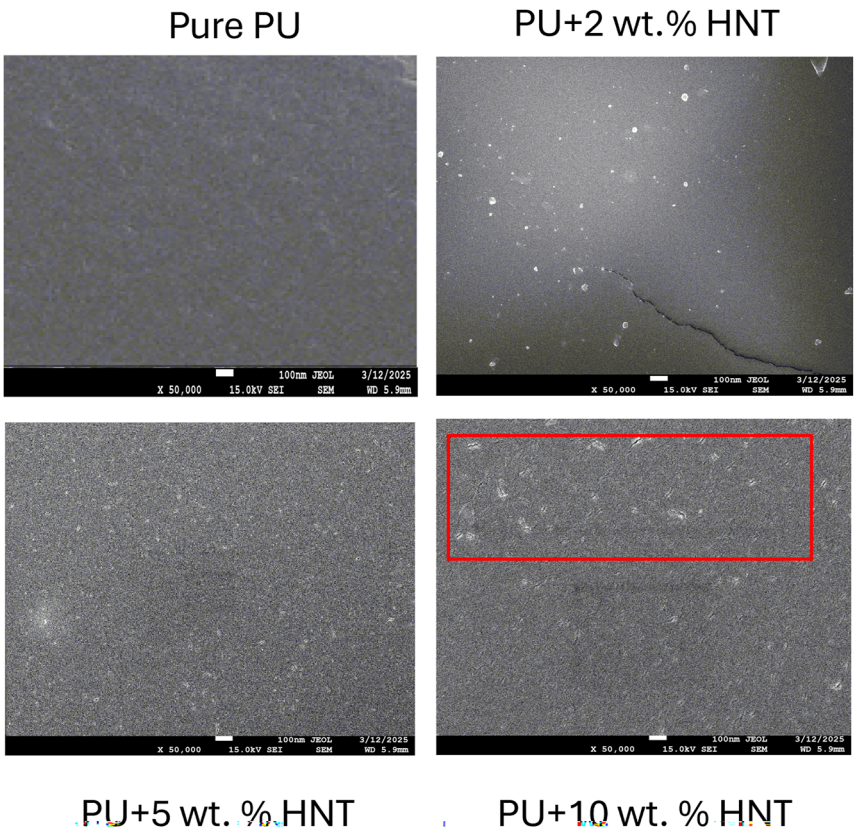

Figure 13: Representative SEM micrographs of fractured surfaces for PU/HNT nanocomposites at varying HNT contents (top-left: 0 wt%, top-right: 2 wt%, bottom-left: 5 wt%, bottom-right: 10 wt%). All images captured at 50,000× magnification, 15.0 kV, scale bar = 100 nm.

mechanical properties. The results confirm that 5 wt% represents an optimal balance between filler loading and interfacial control, while higher concentrations introduce microstructural defects that degrade multifunctional performance.

4 Conclusions

This study systematically investigated the dielectric, thermal, and mechanical performance of PU nanocomposites doped with HNT, emphasizing their applicability as advanced electroinsulating materials. Experimental analysis of commercial 2C cold-curing PU formulation was employed to ensure its industrial relevance, while maintaining standard working procedures for the preparation of nanocomposite systems.

The experimental results showed a strong dependence of the multifunctional properties on HNT loading. At concentration (2 wt%), HNT improved the Young's modulus, tensile strength, and suppression of dielectric loss due to enhanced interfacial interactions and chain mobility, while maintaining thermal conductivity comparable to pure PU. At concentrations (5 wt%), an optimal balance was achieved: dielectric permittivity was significantly enhanced via interfacial (Maxwell–Wagner–Sillars) polarization, volume resistivity increased by nearly 17-fold, and thermal conductivity showed a statistically significant improvement, while mechanical metrics such as Young's modulus and tensile strength were maximized. However, incorporating (10 wt%) led to HNT agglomeration, as confirmed by SEM and ^{27}Al NMR, which introduced localized heterogeneity and resulted in reduced mechanical performance and dielectric stability.

The BDS analysis, interpreted through the Havriliak–Negami model, provided deeper insight into relaxation dynamics. The observed asymmetric broadening of dielectric loss peaks indicated multiple coexisting relaxation mechanisms, with interfacial polarization and chain mobility strongly dependent on concentration of HNT and dispersion quality. These findings confirm that interfacial are is the key factor in tuning dielectric performance.

In summary, the results demonstrate that the rational integration of HNT into 2C PU matrix (VUKOL N22 Magna) enables the design of multifunctional nanodielectrics that combine high volume resistivity, tunable dielectric permittivity, moderate thermal conductivity enhancement, and improved mechanical strength. The study successfully points out the state of the art by bridging between laboratory-scale HNT studies and industrial 2C cold-curing PU systems, highlighting the potential of naturally abundant nanotubular fillers for next-generation electroinsulating, encapsulation, and energy storage applications.

Funding information: This research was supported by the Slovak Research and Development Agency under contract No. APVV-21-0078.

Author contributions: All authors have accepted responsibility for the entire content of this manuscript and approved its submission.

Conflict of interest: The authors state no conflict of interest.

Data availability statement: All data generated or analysed during this study are included in this published article.

References

1. Bertolino V, Cavallaro G, Milioto S, Parisi F, Lazzara G. Thermal properties of multilayer nanocomposites based on halloysite nanotubes and biopolymers. J Compos Sci 2018;2:41.
2. Kushwaha SKS, Kushwaha N, Pandey P, Fatma B. Halloysite nanotubes for nanomedicine: prospects, challenges and applications. *BioNanoScience* 2021;11:200–8.
3. Chen S, Yang S, Chen S, Zuo F, Wang P, Li Y, et al. Polyarylene ether nitrile dielectric films modified by HNTs@PDA hybrids for high-temperature resistant organic electronics field. Nanotechnol Rev 2023; 12:20230117.
4. Iroegbu AOC, Ray SS. Recent developments and future perspectives of biorenewable nanocomposites for advanced applications. Nanotechnol Rev 2022;11:1696–721.
5. Cheng C, Song W, Zhao Q, Zhang H. Halloysite nanotubes in polymer science: purification, characterization, modification and applications. Nanotechnol Rev 2020;9:323–44.
6. Hornak J, Kadlec P, Polanský R. Halloysite nanotubes as an additive to ensure enhanced characteristics of cold-curing epoxy resins under fire conditions. Polymers 2020;12:1881.
7. Khan ZI, Mohsin MEA, Habib U, Mousa S, Hossain SS, Ali SS, et al. Enhanced mechanical and thermal performance of sustainable RPET/PA-11/Joncryl® nanocomposites reinforced with halloysite nanotubes. Polymers 2025;17:1433.
8. Lapčík L, Sepetcioğlu H, Murtaja Y, Lapčíková B, Vašina M, Ovsík M, et al. Study of mechanical properties of epoxy/graphene and epoxy/halloysite nanocomposites. Nanotechnol Rev 2023;12:20220520.
9. Fahimizadeh M, Wong LW, Baifa Z, Sadjadi S, Auckloo SAB, Palaniandy K, et al. Halloysite clay nanotubes: innovative applications by smart systems. Appl Clay Sci 2024;251:107319.
10. Kim W, Yoon G, Kim J, Jeong H, Kim Y, Choi H, et al. Thermally-curable nanocomposite printing for the scalable manufacturing of dielectric metasurfaces. Microsystems & Nanoengineering 2022;8:73.
11. Zare Y, Munir MT, Rhee KY. Tensile modulus of polymer halloysite nanotubes nanocomposites assuming stress transferring through an imperfect interphase. Sci Rep 2024;14:23219.
12. Chen J, Shen Z, Zhao Y, Liu X, Chen F, Liu J. Aligning halloysite nanotubes in elastomer toward flexible film with enhanced dielectric constant. Compos Commun 2024;52:102140.
13. Thomas J, Thomas PS, Stephen R. Improved mechanical, thermal, and barrier properties of halloysite nanotubes and nanocellulose

incorporated PVA-PEO films: for food packaging applications. Food Packag Shelf Life 2024;46:101373.
14. Habib U, Khan ZI, Mohamad ZB. Compatibility and miscibility of recycled polyethylene terephthalate/polyamide 11 blends with and without joncryl® compatibilizer: a comprehensive study of mechanical, thermal, and thermomechanical properties. Iran Polym J (Engl Ed) 2024;33:1313–26.
15. Yousefi MA, Rahmatabadi D, Baniassadi M, Bodaghi M, Baghani M. 4D printing of multifunctional and biodegradable PLA-PBAT-Fe_3O_4 nanocomposites with supreme mechanical and shape memory properties. Macromol Rapid Commun 2024;46:2400661.
16. Rahmatabadi D, Yousefi MA, Shamsolhodaei S, Baniassadi M, Abrinia K, Bodaghi M, et al. 4D printing of polyethylene glycol-grafted carbon nanotube-reinforced polyvinyl chloride–polycaprolactone composites for enhanced shape recovery and thermomechanical performance. Adv Intell Syst 2025;7:2500113.
17. Yang M, Guo M, Xu E, Ren W, Wang D, Li S, et al. Polymer nanocomposite dielectrics for capacitive energy storage. Nat Nanotechnol 2024;19:588–603.
18. Guo F, Aryana S, Han Y, Jiao Y. A review of the synthesis and applications of polymer–nanoclay composites. Appl Sci 2018;8:1696.
19. Vahedi V, Pasbakhsh P. Instrumented impact properties and fracture behaviour of epoxy/modified halloysite nanocomposites. Polym Test 2014;39:101–14.
20. Polanský R, Kadlec P, Slepička P, Kolská Z, Švorčík V. Testing the applicability of LDPE/HNT composites for cable core insulation. Polym Test 2019;78:105993.
21. Khan ZI, Habib U, Mohamad ZB, Tufail A, Raji AM, Khan AU. Innovative hybrid nanocomposites of recycled polyethylene terephthalate/polyamide 11 reinforced with sepiolite and graphene nanoplatelets. J Thermoplast Compos Mater 2024;38:1063–88.
22. Khan ZI, Habib U, Mohamad ZB, Khan I. Mechanical and thermal properties of a newly developed sepiolite filler-filled rPET/PA11 thermoplastic nanocomposites. Results Eng 2024;21:101731.
23. Uddin A, Estevez D, Khatoon R, Qin F. Thermally stable silicone elastomer composites based on MoS_2@Biomass-Derived carbon with a high dielectric constant and ultralow loss for flexible microwave electronics. ACS Appl Mater Interfaces 2023;15:27144–55.
24. Ai D, Chang Y, Liu H, Wu C, Zhou Y, Han Y, et al. Dielectric nanocomposites with superb high-temperature capacitive performance based on high intrinsic dielectric constant polymer. Nano Res 2024;17:8504–12.
25. Wang X, Jang SC, Lee JH, Park J, Noh B, Choi H, et al. Ultraflexible and tough nanodielectric films with high-temperature resilience for harsh-environment energy storage. Adv Funct Mater 2024;34:2405530.
26. Hardoň Š, Kúdelčík J, Baran A, Trnka P, Michal O, Tamus A, et al. Fabrication and broadband dielectric study of properties of nanocomposites materials based on polyurethane. IEEE Access 2024; 12:114227–41.
27. Hardoň Š, Kúdelčík J, Baran A, Michal O, Trnka P, Hornak J. Influence of nanoparticles on the dielectric response of a single component resin based on polyesterimide. Polymers 2022;14:2202.
28. Hornak J, Černohous J, Prosr P, Rous P, Trnka P, Baran A, et al. A comprehensive study of polyurethane potting compounds doped with magnesium oxide nanoparticles. Polymers 2023;15:1532.
29. Kúdelčík J, Hardoň Š, Trnka P, Michal O, Hornak J. Dielectric responses of polyurethane/zinc oxide blends for dry-type cast cold-curing resin transformers. Polymers 2021;13:375.
30. Kúdelčík J, Hardon S, Hockicko P, Kudelcikova M, Hornak J, Prosr P, et al. Study of the complex permittivity of a polyurethane matrix modified by nanoparticles. IEEE Access 2021;9:49547–56.
31. Merck KGaA, Darmstadt, Germany and/or its affiliates. Halloysite nanotubes, product no. 685445; 2025. https://www.sigmaaldrich.com/SK/en/product/aldrich/685445 [Accessed 28 July 2025].
32. VUKI a.s. Download center – Technical documentation; 2025. https://www.vuki.sk/na-stiahnutie [Accessed 28 July 2025].
33. Michal O, Mentlík V, Hornak J. Impact of ultrasonic mixing on the electrical properties of PEI/SiO_2 nanocomposites. In: AIP Conference Proceedings. AIP Publishing; 2021, vol 2411. 1:050010 p.
34. Pei A, Chen Q, Zhao Y, Liang Y, Wang H, Xu J, et al. Effect of interfacial hydrogen bonding on phase separation and segmental dynamics in polyurethane nanocomposites. Macromolecules 2011;44:3604–13.
35. Baran A, Hardoň Š, Kúdelčík J, Hornák J, Trnka P. Effect of halloysite nanotubes on dielectric and mechanical properties of polyurethane nanocomposites. In: AIP Conference Proceedings, Forthcoming, accepted for publication. American Institute of Physics; 2025. Available from: http://kf.elf.stuba.sk/~apcom/sprogram/pdf/BARAN.pdf.
36. Le Ba T, Alkurdi AQ, Lukács IE, Molnár J, Wongwises S, Gróf G, et al. A novel experimental study on the rheological properties and thermal conductivity of halloysite nanofluids. Nanomaterials 2020;10:1834.
37. Lue SJ, Ou JS, Kuo CH, Chen HY, Yang TH. Pervaporative separation of azeotropic methanol/toluene mixtures in polyurethane–poly(dimethylsiloxane) (PU–PDMS) blend membranes: correlation with sorption and diffusion behaviors in a binary solution system. J Membr Sci 2010;347:108–15.
38. Stanciu A, Airinei A, Timpu D, Ioanid A, Ioan C, Bulacovschi V. Polyurethane/polydimethylsiloxane segmented copolymers. Eur Polym J 1999;35:1959–65.
39. Lei W, Fang C, Zhou X, Cheng Y, Yang R, Liu D. Morphology and thermal properties of polyurethane elastomer based on representative structural chain extenders. Thermochim Acta 2017;653:116–25.
40. Lei W, Fang C, Zhou X, Li J, Yang R, Zhang Z, et al. Thermal properties of polyurethane elastomer with different flexible molecular chain based on para-phenylene diisocyanate. J Mater Sci Technol 2017;33:1424–32.
41. Zia KM, Bhatti IA, Barikani M, Zuber M, Bhatti HN. XRD studies of polyurethane elastomers based on chitin/1,4-butane diol blends. Carbohydr Polym 2009;76:183–7.
42. Parvathi K, Ramesan MT. Tailoring the structural, electrical and thermal properties of zinc oxide reinforced chlorinated natural rubber/poly (indole) blend nanocomposites for flexible electrochemical devices. J Polym Res 2023;30:55.
43. Kadi S, Lellou S, Marouf-Khelifa K, Schott J, Gener-Batonneau I, Khelifa A. Preparation, characterisation and application of thermally treated Algerian halloysite. Microporous Mesoporous Mater 2012;158:47–54.
44. Abotaleb A, Gladich I, Mroue K, Abounahia N, Alkhateeb A, Al-Shammari A, et al. Impact of thermal treatment on halloysite nanotubes: a combined experimental-computational approach. Heliyon 2024;10:e39952.
45. Abdullah NAS, Mohamad Z, Khan ZI. Thermo-mechanical properties and optimization of sodium alginate as a polymer backbone substrate for biosensor application. Environ Qual Manag 2024;34:e22242.
46. Kúdelčík J, Hardon S, Hockicko P, Kudelcikova M, Hornak J, Prosr P, et al. Study of the complex permittivity of a polyurethane matrix modified by nanoparticles. IEEE Access 2021;9:49547–56.
47. Nelson JK. Dielectric polymer nanocomposites. New York: Springer; 2004.

48. International Electrotechnical Commission. IEC 62631-2-1: 2018 – dielectric and resistive properties of solid insulating materials – part 2-1: determination of permittivity and dissipation factor – AC methods; 2018. Standard by IEC, Geneva, Switzerland. Available from: https://webstore.iec.ch/publication/29583.
49. Adamczyk M, Rok M, Wolny A, Orzechowski K. Dielectric properties of halloysite and halloysite-formamide intercalate. J Appl Phys 2014;115: 024101.
50. Liu D, Hoang AT, Pourrahimi AM, Pallon LKH, Nilsson F, Gubanski SM, et al. Influence of nanoparticle surface coating on electrical conductivity of LDPE/Al_2O_3 nanocomposites for HVDC cable insulations. IEEE Trans Dielectr Electr Insul 2017;24:1396–404.
51. Pourrahimi AM, Olsson RT, Hedenqvist MS. The role of interfaces in Polyethylene/metal-oxide nanocomposites for ultrahigh-voltage insulating materials. Adv Mater 2018;30:1703624.
52. Džunuzović JV, Stefanović IS, Džunuzović ES, Kovač TS, Malenov DP, Basagni A, et al. Fabrication of polycaprolactone-based polyurethanes with enhanced thermal stability. Polymers 2024;16:1812.
53. Wendou D, Jiaxin L, Jia T, Zhengxiang W, Shuhong F. A review of recent development in preparation and modification of waterborne polyurethanes and their application in waterborne inks for plastic packaging printing. J Coating Technol Res 2025;22:1301–29.
54. Elabbasy MT, Samak MA, Saleh AA, El-Shetry ES, Almalki A, El-Morsy M, et al. Enhancement of wound dressings through cerium canadate and hydroxyapatite-infused hyaluronic acid and PVA membranes: a comprehensive characterization and biocompatibility study. Mater Chem Phys 2024;328:129972.
55. Cimbala R, Havran P, Király J, Rajňák M, Kurimský J, Šárpataky M, et al. Dielectric response of a hybrid nanofluid containing fullerene C60 and iron oxide nanoparticles. J Mol Liq 2022;359:119338.
56. Havran P, Cimbala R, Dolník B, Rajňák M, Štefko R, Király J, et al. Dielectric relaxation spectroscopy of hybrid insulating nanofluids in time, distribution, and frequency domain. J Mol Liq 2024;409: 125409.
57. Tarnacka M, Hachuła B, Geppert-Rybczyńska M, Zięba A, Kamiński K. Dielectric studies on the dynamics of two van der Waals liquids differing in the ring rigidity confined within mesoporous silica. J Mol Liq 2025;437:128517.
58. Mentlík V, Michal O. Influence of SiO_2 nanoparticles and nanofibrous filler on the dielectric properties of epoxy-based composites. Mater Lett 2018;223:41–4.
59. Velayutham TS, Abd Majid WH, Gan WC, Khorsand Zak A, Gan SN. Theoretical and experimental approach on dielectric properties of ZnO nanoparticles and polyurethane/ZnO nanocomposites. J Appl Phys 2012;112:054106.
60. Ersoy A, Atalar F, Hiziroğlu H. A study on particle size effect of polyurethane-mica composites. IEEE Access 2024;12:679–88.
61. Janek M, Kudelcik J, Hardon S, Gutten M. Novel experimental setup for measuring the thermal conductivity of polyurethane composites with various nanoparticle contents. Sensors 2024; 24:7269.
62. Lin C, Ying P, Huang M, Zhang P, Yang T, Liu G, et al. Processable and recyclable polyurethane/HNTs@Fe_3O_4 solid-solid phase change materials with excellent thermal conductivity for thermal energy storage. Polym Compos 2021;42:6813–23.
63. Kang M, Liu Y, Lin W, Liang C, Cheng J. The thermal behavior and flame retardant performance of phase change material microcapsules with halloysite nanotube. J Energy Storage 2023;60:106632.
64. Liu Y, Kang M, Lin W, Liang C, Wang Y, Zhang F, et al. Improved thermal energy storage, leak prevention and flame retardance of phase change material using halloysite nanotubes. J Therm Anal Calorim 2023;148:9501–10.
65. Mo H, Yang K, Li S, Jiang P. High thermal conductivity and high impact strength of epoxy nanodielectrics with functionalized halloysite nanotubes. RSC Adv 2016;6:69569–78.
66. International Organization for Standardization. ISO 527-1:2019: plastics – determination of tensile properties – part 1: general principles; 2019. https://www.iso.org/standard/75828.html [Accessed July 2025].
67. Joussein E, Petit S, Churchman J, Theng B, Righi D, Delvaux B. Halloysite clay minerals: a review. Clay Miner 2005;40:383–426.
68. Du M, Guo B, Jia D. Thermal stability and flame retardant effects of halloysite nanotubes on poly(propylene). Eur Polym J 2006;42: 1362–9.
69. Ray SS, Okamoto M. Polymer/layered silicate nanocomposites: a review from preparation to processing. Prog Polym Sci 2003;28: 1539–641.
70. Leite AJ, de Oliveira AD. Mechanical and thermal properties of polyurethane composites reinforced with halloysite nanotubes. Mater Res 2015;18:269–75.
71. Kausar A. Review on polymer/halloysite nanotube nanocomposite. Polym Plast Technol Eng 2017;57:548–64.